5. π-Decay, μ-Capture and Bunching Section

5.1 Introduction

Following the target, each proton bunch from the four bunches extracted from the proton driver produces a cloud of pions that is transported downstream within a focusing channel, where the pions decay to muons following $\pi \rightarrow \mu + \nu$. The initial pions, and the product muons, are produced with a large energy spread. Due to this energy spread the length of the beam bunch increases in this transport and a longitudinal position-energy correlation develops with the lower-energy end of the beam trailing behind the higher-energy muons. This energy spread is much larger than the acceptance of the following cooling system. The plan is to reduce this energy spread by an acceleration system that decelerates the high-energy head of the bunch while accelerating the low-energy tail, obtaining at the end of this "phase-rotation" system a beam with minimal energy spread and a relatively long bunch length.

In the previously developed μ^+-μ^- collider scenarios [1], the phase-rotation system was constrained by the need to keep the entire muon beam from an initial proton bunch within a single bunch throughout the system. The bunch length had to be short, in order to fit into the longitudinal acceptance of the cooling and bunching system which was based on ~30MHz rf. For a neutrino source, the long bunch can be split into a string of higher-frequency bunches (with that frequency matched to the following acceleration systems) [1].

In the ν-source, a phase-rotation system is used to obtain a very long bunch and that greater length coupled with a long acceleration pulse (obtained from an induction linac) obtains a much-reduced energy spread. The long bunch is then inserted into an RF system, which forms the beam into 201.25 MHz bunches matched to the following cooling system. A design goal of the present scenario is to obtain an energy spread small enough so that the following cooling system can capture and cool a maximal number of muons without any additional energy cooling.

5.2 Baseline Scenario Description

A schematic overview of the precooling decay, RF capture and bunching section is displayed [2] in Figure 1. It shows a 50m decay channel following the target and capture solenoid. This channel is matched into an induction linac phase-energy rotation system (100m long), which is followed by a "minicool" energy absorber (2.45m of liquid hydrogen), and a bunching section (16.4m long) matching the beam into a 201.25 MHz cooling system. Simulation results are displayed in Table 1.

A critical parameter for this channel is the total voltage difference that can be provided by the induction linac, since that also determines the energy range which can be accepted by the capture system. Our baseline scenario contains a voltage difference of 200 MV (+150 to –50 MV). With that range, we can accept the $\pi \rightarrow \mu$ particles with energies centered about the maximal production energy of ~130 MeV kinetic energy, obtaining an acceptance range of about 30 to 230 MeV. The transverse focusing magnets and the apertures are selected to accept most of the particles produced within that energy range. The acceptance of the overall system is matched to the precooling design goal, which is to provide ~0.1μ per initial proton from the target to the cooling system, and our simulations

Region	**Position**	**π+μ/proton**	**E-window**	**$\varepsilon_{t,n}$(mm)**	**σ_x(m)**	**σ_{px}(MeV/c)**
After Target	0	0.242	<500 MeV	15.1	0.090	23.0
Decay Channel	47 m	0.226	<500 MeV	15.9	0.092	22.5
Matching (D)	50 m	0.222	<500 MeV	16.5	0.057	34.2
Induction Linac	150 m	0.191	<450 MeV	16.3	0.060	44.9
"Mini-Cool"	153.45 m	0.191	<375 MeV	12.6	0.055	32.6
Buncher(all μ's)	170.9 m	0.188	<375 MeV	12.4	0.046	32.2
Buncher (in bucket)	170.9 m	0.123	In bucket	12.0	0.046	31.4

Table 1: Beam Properties along the Capture and Bunching Section.

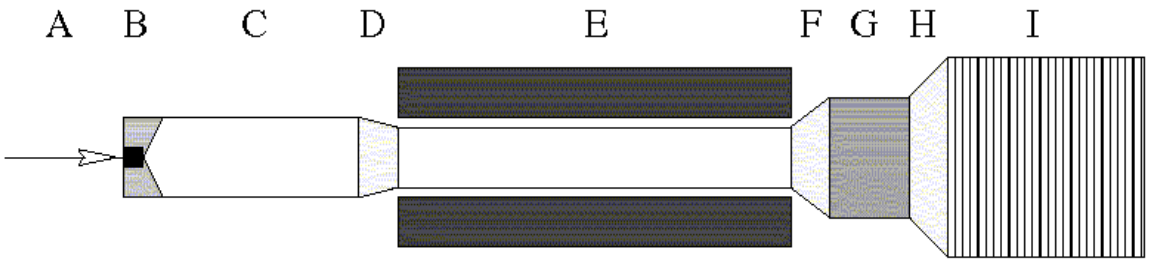

Figure 1: Schematic overview of the $\pi \rightarrow \mu$ production, capture and bunching system, showing:

A: proton beam (16 GeV, 4bunches)
B: Target station (Carbon target)
C: Drift- $\pi \rightarrow \mu$ decay region (L=47 m, B=1.25 T)
D: Matching section (L=3 m)
E: Induction Linac (L=100 m, B_{ave} = 3T, V′ = -0.5—1.5 MV/m)
F. Matching section (L=1 m)
G: Minicooling (2.45m liquid H_2, B = 5 T)
H: Matching section (L=1m)
I: Buncher (L=16.432 m, B=5 T, includes three 2 m RF accelerating cells)
(Lengths of sections are not to scale.)

show that performance at this level should be possible.

In the following subsections we describe the various subcomponents of this "precooling" system in greater detail: the decay channel, the induction linac, the minicooling section and the buncher, and discuss matching into the following cooling section. Results of tracking simulations will be presented to estimate the performance of the various sections [2][3]. The simulation results are summarized in Table 1 and these results are discussed in the remainder of the chapter.

5.2.1 The Decay Channel

As discussed in the previous section, in the baseline scenario 16 GeV proton beam bunches collide with a 0.8m long graphite (C) target, that is immersed in a 20 T solenoidal focusing field. π's produced in the target are captured in the solenoidal field and directed into a decay channel for $\pi \rightarrow \mu + \nu$ decay. The focusing solenoidal field is gradually reduced to 1.25 T over a ~3m transition region, while the transport region radius is increased to 30cm. At the end of transition region ~0.242 π + μ per initial proton are both within the energy acceptance cut (E < 500 MeV) and captured within the transport. The rms transverse emittance matched into the decay channel is ~15 mm, corresponding to a beam size of $\sigma_x = \sigma_y \cong 9$ cm, and $\sigma_{Pt} \cong 30$ MeV/c. The decay channel immediately follows this transition region.

The decay channel consists simply of a long large-diameter beam pipe with a 30cm radius and with a solenoidal focusing field of 1.25 T. In the present baseline, the total length of this decay channel is 50 m, including a final 3 m subsection for matching into the following induction linac.

By the end of the 50m decay channel section, ~95% of the π's in the initial beam have decayed to μ's. Simulations show that very few (< ~10%) of the initially captured π + μ's (compared to 3 m after the target) are lost in this section. The transverse momentum introduced by decay is smaller than the intrinsic beam momentum spread and adds little to the beam emittance. The transverse emittance increase is only ~10% to $\varepsilon_{t,rms} \cong 16.5$ mm.

Figure 2 shows projections of the beam phase space distribution at the end of the decay channel. The initial energy spread of ~300 MeV is stretched over a ~50 m length. The transverse phase space projections (x-P_x and x-P_y) are also displayed.

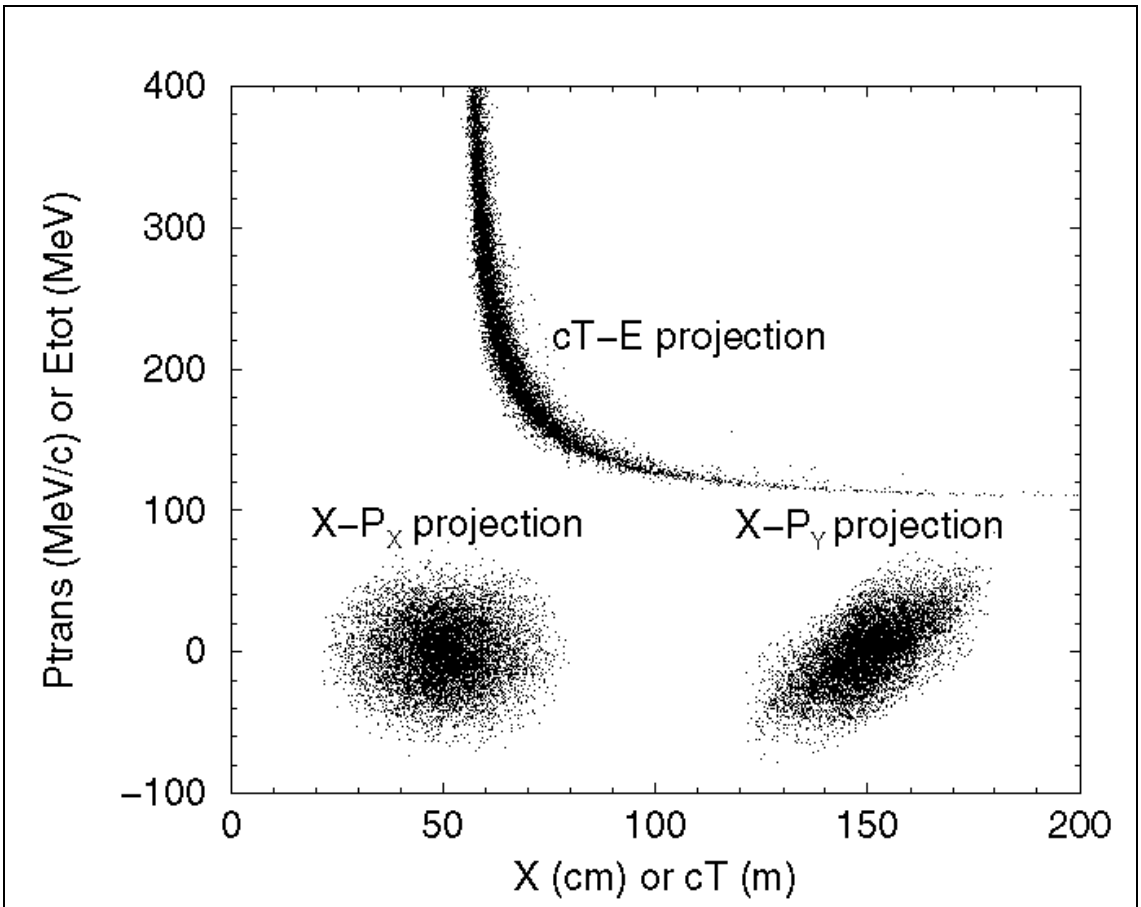

Figure 2: Beam at the end of the 47 m decay channel. Three projections of the 6-D phase space distributions of a simulated beam are displayed. The cT-E projection shows the energy-dependent bunch lengthening. The X-P_x projection indicates the beam phase-space size ($\sigma_x \cong 9$ cm, $\sigma_{Px} \cong 22$ MeV/c). The X-P_y projection indicates the beam angular momentum associated with the 1.25T solenoidal focusing field.

At the end of the decay channel the focusing magnetic field is gradually increased from 1.25 T to 3 T over a 3m length, while the beam transport radius is reduced from 30 cm to 20 cm. This change matches the beam dimensions and focusing system to that used in the following induction linac capture system. Figure 3 shows a cross section of this matching section. The rms beam size is reduced from $\sigma_x = \sigma_y = 9$ cm in the decay channel to ~5.7 cm at the end of the matching section. This fits easily within the 20 cm radius aperture of the induction linac.

5.2.2 The Induction Linac

The decay channel is followed by an induction linac. The channel consists of 100 1m modules of the form displayed schematically in Figure 4. Each module has an accelerating gap of 10cm, which provides an accelerating voltage of between –0.5 and 1.5 MV to the particles. The focusing, longitudinal magnetic field is provided by an array of superconducting solenoids placed in separate cryostats inside the induction modules. The gaps between the cryostats are shaped to serve as accelerating gaps

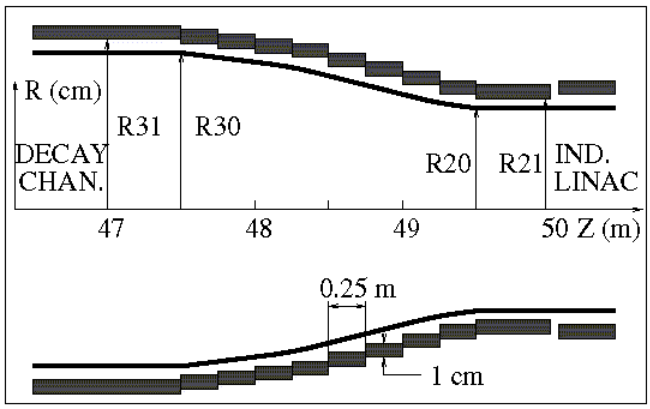

Figure 3: The 3m long matching section between decay channel and induction linac. Focusing solenoidal field increases gradually from 1.25T to 3T, while the aperture reduces from 30cm radius to 20cm radius.

Figure 4 shows cylindrical coils with 22.2 cm inner radius and 1.46 cm thickness separated by the induction gap of 14 cm length and spacers of length a. Cylindrical magnetic induction cores surround these coils. The coils provide a mean focusing of 3 T on axis, with a periodic fluctuation of ~10% due to the coil position. The 1 m, ~3 T periodic focusing system has betatron oscillation resonance's for ~200 MeV/c particles, which would lead to particle losses. However, these resonances are eliminated if the inter-coil spacing length is chosen to be a=14cm, the same as the induction gap coil spacing. This changes the transverse focusing period to 0.5m and removes the medium energy resonance condition [2]. A preliminary engineering layout of an integrated superconducting coil will be discussed later on (see also Figure 12).

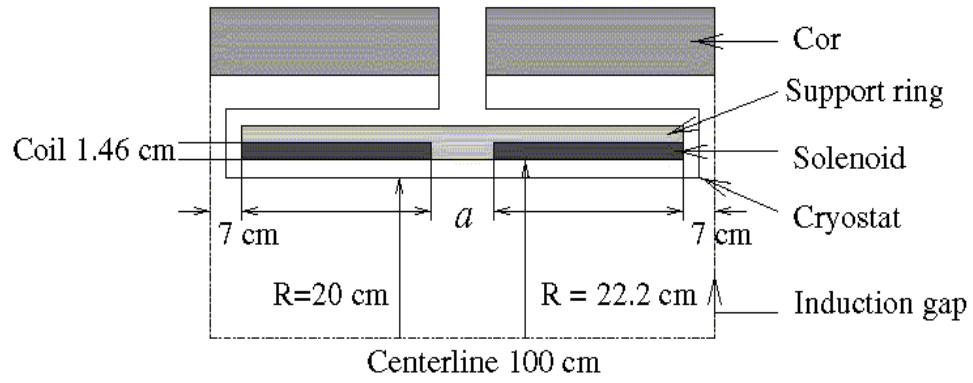

Figure 4: Schematic cross section of an induction linac cell.

The cores are excited by a waveform matched to the beam energy-phase distribution, with a voltage range from –0.5 MV/gap for the high-energy head of the bunch to ~1.5 MV for the low energy tail. This asymmetric form, which accelerates the beam centroid by ~0.5 MV/gap, was chosen as a preferred mode for the pulse forming network, since it facilitates a fast reset of the cores, which enables sequential very fast excitation of the 4 primary bunches [3][4]. The pulse lengthens from 150 ns to 200 ns along the linac, matching the bunch lengthening. Figure 5 shows the desired module waveforms along the linac (from gap 1 to 100).

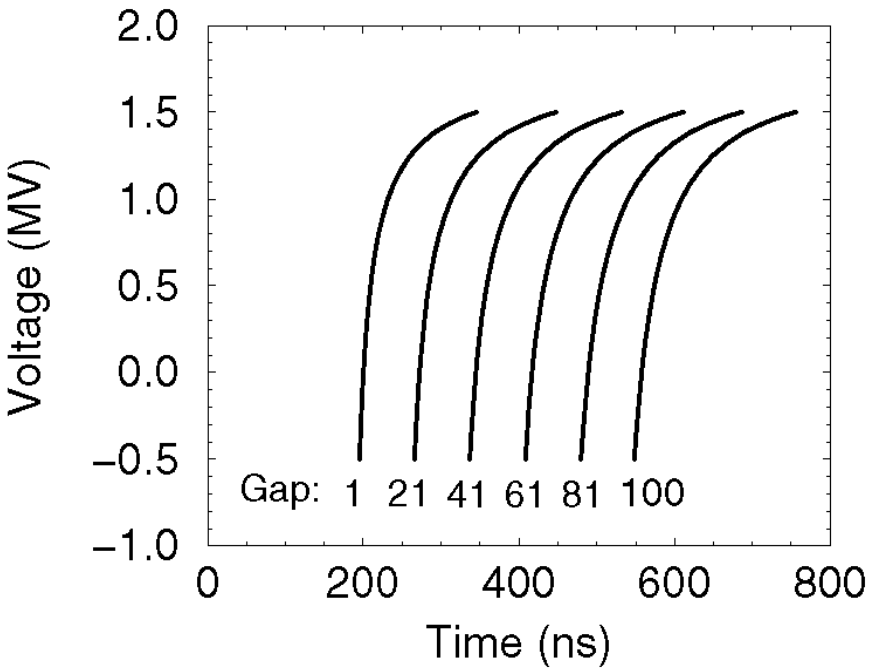

Figure 5: Induction Linac waveforms along the induction linac. Pulses for gaps 1, 21, 61, 81, and 100 are displayed.

Energy-phase distributions of the beam along the induction linac are displayed in Figure 6. The bunch lengthening with energy spread flattening of the captured beam is displayed. A core of a beam with a full energy width of ~300 MeV and a bunch length of ~50 m (with a curved position-energy correlation) is phase rotated into a ~80 m long bunch centered about ~280 MeV beam energy (~175MeV kinetic energy) with a full-width of ~100 MeV. The

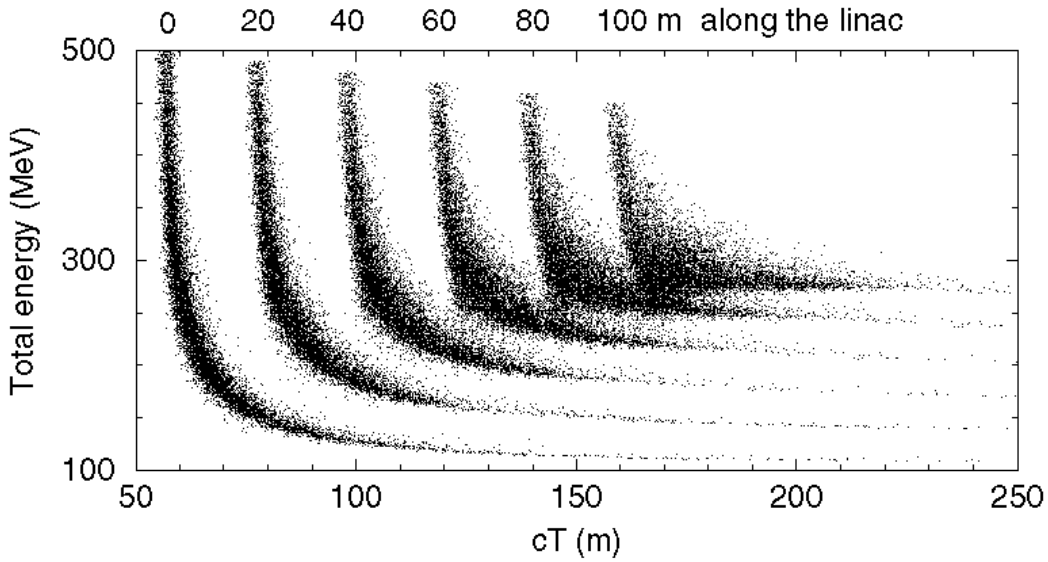

Figure 6: Beam distributions in E-cT phase space along the induction linac. Distributions from L = 0, 20, 40, 60, 80, and 100 m are shown.

width is correlated with position along the bunch, but the mean beam energy is not. About 10% of the initial beam is lost in the transport. The beam transverse emittance and beam size are approximately unchanged in the RF rotation. The rms transverse emittance ε_T remains at ~16 mm (rms, normalized) while the beam radius remains $\sigma_x \cong 6$ cm.

In the baseline design a string of 4 proton bunches, spaced by ~500 ns, is sent onto the target. The induction cells must provide approximately identical waveforms for the muons from each proton bunch coming from the proton driver. Thus, the induction cells must be driven by a 4-pulse waveform, with each pulse ~150—200 ns long, spaced by 500 ns. Note that the four-pulse design at these parameters was selected because it is estimated that this was within demonstrated induction linac capabilities [6]. The induction linac itself will be discussed in greater detail later on in this chapter.

5.2.3 "Minicool" Absorber Section

At the end of the induction linac the mean beam kinetic energy is $T_\mu \sim 175$ MeV (total energy $E_\mu \cong 280$ MeV), while the following bunching and cooling section is designed for muons with a kinetic energy of ~100 MeV. In order to match these central energies the beam passes through an energy-loss absorber. This absorber also provides some transverse cooling.

Following the induction linac a 3 m transition region is placed with coils matching the beam optics into a solenoidal magnetic field of 5 T at the absorber. The physical aperture is increased to a radius of 30cm to minimize possible losses. The absorber is a 2.45 m long liquid H_2 bottle, which lowers the mean beam kinetic energy from 175 MeV to 100 MeV. Simulations show that this insert decreases the rms transverse emittance $\varepsilon_{t,rms}$ from 16.4 mm to 12.4 mm. However, the rms energy spread is somewhat increased by the absorber. Figure 7 shows the longitudinal (E-cτ) phase space distributions of the beam before and after the minicool insert; the energy spread increase is not large compared to the large intrinsic beam energy spread.

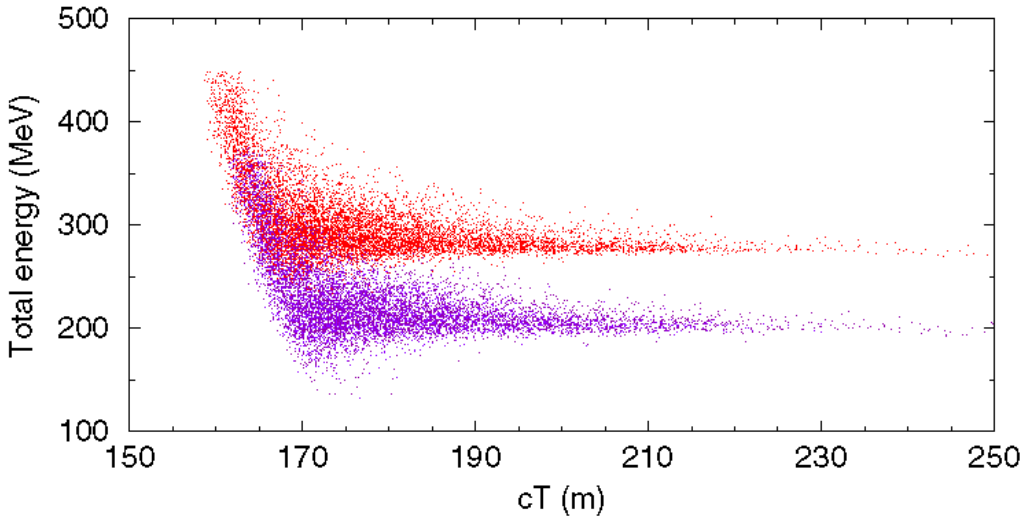

Figure 7: Longitudinal phase space distributions of the μ-beam before (above, red) and after (below, violet) the minicool energy loss insert.

In our baseline scenario the "minicool" energy loss is used primarily to reduce the central energy of the phase-rotated beam to that of the cooling channel, but it also provides some initial transverse cooling. If a longer energy loss section is used, more transverse cooling is obtained and the beam energy could be lowered to the level where an adiabatic capture and acceleration with a 201.25 MHz section can match the beam energy to the cooling rf. However, at present parameters the energy spread of the beam is initially large and energy loss at low energies

would increase that energy spread far beyond the acceptance of the cooling channel. This limitation could be removed if energy cooling were incorporated into the scenario.

5.2.4 Buncher

After the mean energy is reduced by the "minicool" absorber to the cooling kinetic energy of $T_\mu \cong 120$ MeV ($P_\mu \cong$ 200 MeV/c), the bunches from the induction linac must be formed into 200 MHz bunches. Several scenarios for transforming a long-bunch beam from the induction linac into a string of short bunches have been proposed and these options have been described in [8]. The optimal scenario depends on the beam properties at the exit of the induction linac as well as the beam cooling scenario requirements. Two styles of matching have been considered:

- An adiabatic match obtained by gradual bunching of the beam with 200 MHz RF. This can be done at a fixed energy corresponding to the mean μ capture and cooling energy, or by lowering the energy to a level where the beam longitudinal motion is enhanced, and then bunching and accelerating the beam to cooling energy. An adiabatic match could minimize phase space dilution, and maintain a small longitudinal phase space.

- A short bunching RF section followed by a drift in which bunch length is minimized to match the cooling acceptance. This drift incorporates transverse matching. This option can be modified to include multiple steps (2 or 3).

Since in the baseline scenario (as currently implemented) the beam energy spread (and longitudinal emittance) is large and not well matched to adiabatic scenario parameters, we have decided to minimize length and cost of the buncher by choosing a short buncher scenario as our baseline.

The buncher used in the baseline scenario is displayed schematically in Figure 8. It has a total length of 16.4 m and contains three 1.944m 201.25 MHz RF modules. The longitudinal beam distributions at the end of the buncher are displayed in Figure 9. It shows the longitudinal distribution of the entire beam; the 201 MHz structure can be seen. The energy width of the beam has been increased, but the degree of increase depends upon position along the bunch. The RF system has partially formed the ~80 m long beam distribution into a string of about fifty 201 MHz bunches. Figure 9 also shows the distribution folded over the 201 MHz period. A 201MHz RF bucket corresponding to the estimated acceptance of a $E_\mu \cong 200$ MeV, f=201MHz cooling system is displayed overlapping the distribution. About 2/3 of the μ's are within that acceptance.

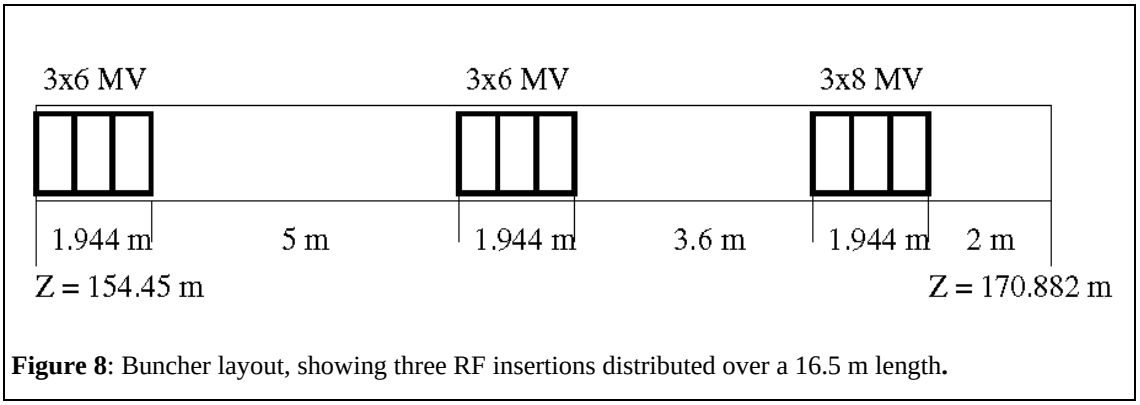

Figure 8: Buncher layout, showing three RF insertions distributed over a 16.5 m length**.**

At the end of the buncher the beam is matched into a 5 T focusing system, and has a transverse emittance of $\varepsilon_{t,rms} \cong$ 12 mm. Longitudinally the beam overflows the expected acceptances of the cooling channel. However, ~0.123 μ per initial proton are within that acceptance, indicating that the precooling section is able to meet the goal of ~0.1 μ/p.

This buncher has not yet been fully optimized. Ref. [8] discusses some of the possible variations, and these will be studied in more detail. Some significant improvements may be expected from future parameter optimization studies, which will include more complete integration with the upstream phase rotation and downstream cooling systems.

5.2.5 Integration with Cooling Section

The optimal beam capture and bunching parameters depend critically on the acceptance and parameters of the downstream cooling and acceleration sections. The cooling channel and some of its design options are described in more detail in the following cooling chapter.

If there is no energy cooling in the scenario, the most critical parameter in downstream acceptance is the longitudinal emittance for the beam entering the cooling channel. A cooling channel has a longitudinal acceptance corresponding to an rf bucket determined by the average accelerating gradient eV′ and stable phase ϕ_0 set such that the energy gain (eV′ $\sin\phi_0$) cancels the mean energy loss rate from absorbers. Figure 9 shows a cooling bucket acceptance superimposed on a simulated μ-distribution. The smaller size of the bucket implies a significant design mismatch.

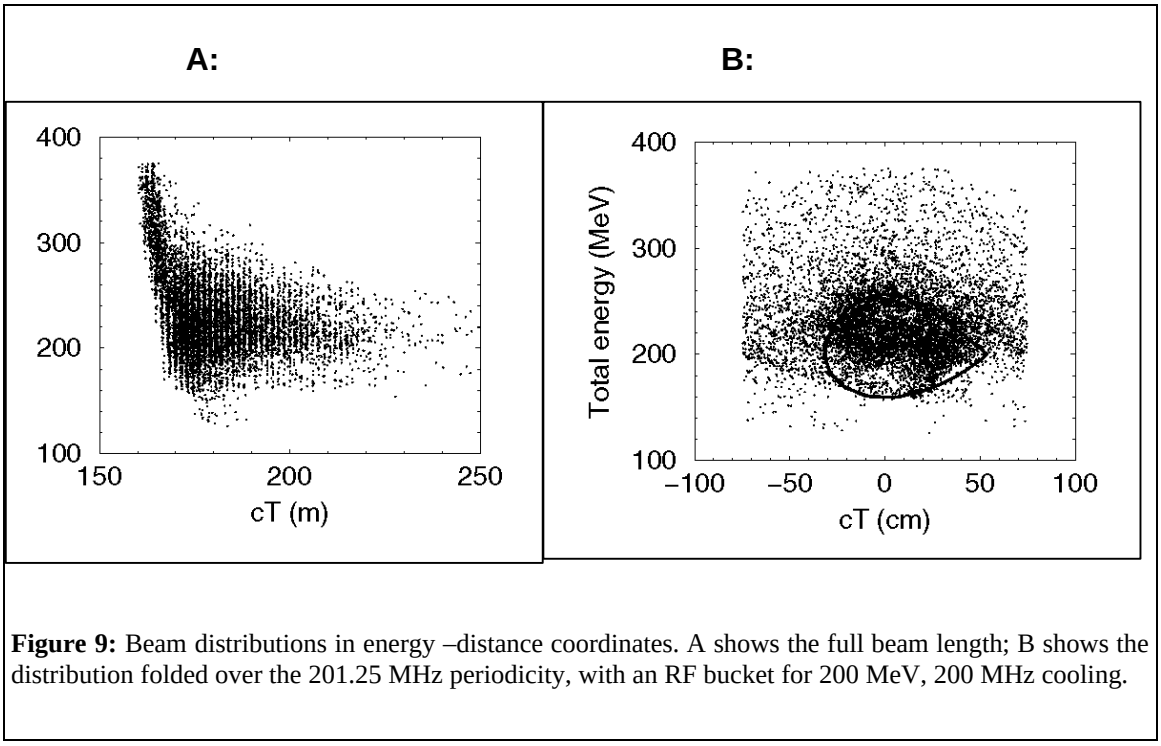

Figure 9: Beam distributions in energy –distance coordinates. A shows the full beam length; B shows the distribution folded over the 201.25 MHz periodicity, with an RF bucket for 200 MeV, 200 MHz cooling.

In the present example we have centered the final beam energy of the precooling section at $E_\mu \cong 200$ MeV, since that is the expected energy for the cooling channel. However it is not known whether that is an optimum cooling energy. A larger longitudinal acceptance with less longitudinal heating would be obtained by a higher energy cooling system; however, it would also have a reduced cooling rate. Variation of the cooling energy within the context of global scenario optimization would be an important goal of future research. Other parameters of the precooling (and cooling) systems may also be varied to improve the match.

5.2.6 Discussion: Variations and Alternatives

A number of variations and improvements on the baseline scenario could be considered and studied. Many of these could improve μ-acceptance. In addition to incremental improvements, greatly different μ-capture scenarios (using different technologies) could be considered. We first consider some incremental improvements.

The present precooling scenario has been shown by simulations to provide ~0.12 μ per initial 16 GeV proton into the acceptance of the cooling channel from an initial Carbon target. Optimization of this scenario should continue with the attempt to increase the yield as much as possible without increasing technical complexity of the system significantly.

One critical parameter (discussed above) is the target material; a high-Z target could provide up to twice as many μ's from the same primary beam. However, because of the much more demanding technology that would be required to build and operate high-Z targets, they are not considered for this study but do provide an obvious upgrade path.

Acceptance could be somewhat improved by increasing the voltage bandwidth of the RF capture system, although the current bandwidth does cover the production peak. Increasing the induction linac voltage range from 200 MV to 300 MV could increase the number of accepted μ's by ~25% but would lengthen the induction linac by 50%.

The energy spread at the end of the precooling region can be reduced by lengthening the decay channel + induction linac system (including lengthening the induction linac pulse beyond 200 ns). In principle the energy spread can be reduced inversely proportional to the final macrobunch width. (For example, A. Van Ginneken has presented a simulation that obtains an energy spread a factor of two smaller, when using a 200 m decay drift together with a 400 ns induction linac pulse. [9])

The energy spread (and longitudinal emittance) at the end of the induction linac, and the subsequent energy spread after the 200MHz buncher, is much larger than desired for the cooling system, and is significantly larger than the longitudinal acceptance of the cooling channel. Thus large particle losses occur at the beginning of the cooling channel. The difficulty is exacerbated by the fact that the cooling system increases the energy spread (and longitudinal emittance), which means increased beam losses in the cooling system. Modification of the capture section to reduce energy spreads (with further scenario optimization and/or more acceleration modules) and modification of the cooling system to include some energy cooling would both be very desirable.

An alternative collection system is described in the PJK scenario [10] and more recently in an updated version of [10]. This scenario begins with a low frequency rf capture section, obtained by 42m of 30—90MHz RF at (~5 MV/m), immediately after the target. This initial capture section obtains a ~1.5m long (rms) μ-bunch with ~15% rms momentum spread. This is followed by an energy loss "minicool" section, a drift section (~100m), and an induction linac (~100m), to obtain a long bunch with much smaller energy spread. Since this system has more total rf capture voltage, and has an initial rf capture section reducing the energy spread closer to the target, the capture efficiency will be larger. Recent calculation indicate [11] that total efficiency could be up to 0.15μ/proton. The final energy spread will be somewhat smaller than our baseline scenario. Also, this RF enables better sorting of the beam polarization, obtaining higher initial μ-beam polarization (25→45% or so). However, the PJK scenario adds significant complexity and power requirement to the capture scenario, requiring development and construction of 30—80 MHz RF systems as well as induction linacs, which will increase risk and cost.

The present scenario uses induction linac systems, which have the great advantage that the acceleration waveform can in principle be tailored to match the phase-energy distribution of the beam, and thereby provide an ideal phase-rotation system. However it is possible that the actual performance of an induction linac system may be deficient in acceleration waveform quality, gradient, reliability, and/or lifetime or simply be too expensive. Alternative acceleration systems such as the ~30 MHz RF system used in the baseline μ^+-μ^- Collider scenarios could be used, without an additional induction linac. Recently scenarios using ~5MHz RF systems (at ~1MV/m) have also been suggested, and are investigated [12]. These (higher-frequency) alternatives may not develop energy spreads as small as those that can be developed from very long induction linac pulses; they may require additional energy cooling in a complete scenario.

5.3 The Technical Design of the Induction Linac

Since the induction linac modules are the primary component of the precooling (phase-energy rotation) system, we include a more detailed discussion of the properties of these modules. Several designs for such an induction linac [4] have been presented and different designs for pulse power production have been studied[5][6]. Figure 10 shows a detailed view of an induction linac module from ref. [4], including acceleration and focusing components. Some parameters are included in Table 2. The 1 m long induction module consists of a set of toroidal magnetic cores surrounding an induction gap. A pulser sends high-current pulses to the module that change the core magnetic fields, and the changing magnetic field generates an accelerating voltage across the induction gap. As compared to

the design discussed in the first part of this chapter technical detail, like for example the exact cell length etc may vary. This is a result of the ongoing optimization with the technical design going on simultaneously.

The induction module includes a 3 T solenoidal field for transverse beam focusing. To minimize the leakage of magnetic field into cores (to < ~0.1 T), the superconducting solenoidal coils are placed inside the cores. It is essential to investigate early on what the maximum tolerable field is going to be at the cores. Separate cryostats and current leads are required for each magnet. A ~20 cm annular gap between the coils and the induction cores is sufficient for cryogenic and magnetic separation.

A number of materials can be considered for the magnetic cores of the induction modules, such as Finemet, Metglas and nanocrystalline compounds. In the baseline design of ref. [4] Finemet and Metglas 2605 are preferred materials.

PARAMETER	VALUE	UNIT
Induction linac length	110	m
Length of induction modules	1	m
Acceleration Gap	0.1	m
Induction pulse length	150—200	ns
Induction pulse voltage	-0.5—1.5	MV
Pulse structure	15×4	Hz × pulses
Induction core material	Finemet or Metglas 2605C	
Core inner radius	45	cm
Core outer radius	77	cm
Core cross section (L=6 cm)	300	cm^2
Core magnetic field change (ΔB)	1	T
Amount of Metglas (100 m)	500000	kg
Peak pulsed power /1 m module	5.5	GW/m
cw Power requirements (100 m)	5	MW
Solenoidal Focusing Field	3	T
Beam Channel aperture	20	cm

Table 2: General Parameters for the Induction Linac.

5.3.1 Overall Topology

Each Induction Linac cell is 1m long operated at 2.00 MeV (-0.50 MeV, +1.50 MeV _ head to tail). This allows the pulsed power pulse train to be delivered to the 10 induction cores per cell at 150 kV, a reasonable voltage level for cables. The cathode of the accelerating gap is located upstream to provide the proper polarity to the beam, but the center conductor of the cables are connected to the cores in the sense that allows the pulse generator to operate in negative polarity, which minimizes the size of its components. The configuration of the major cell components was dictated by the need to maintain a high acceleration gradient at conservative electric field stress levels on the vacuum insulator and cathode surfaces in vacuum, and to minimize the perturbation of the axial magnetic field of the superconducting magnets caused by the acceleration gap. A 1 m long inter-cell module is positioned every 10 cells to provide vacuum pumping for the beam tube and beam position/net current monitors. A constant solenoid gap pitch is maintained by choosing the inter-cell module length to be the same as that of the acceleration cells.

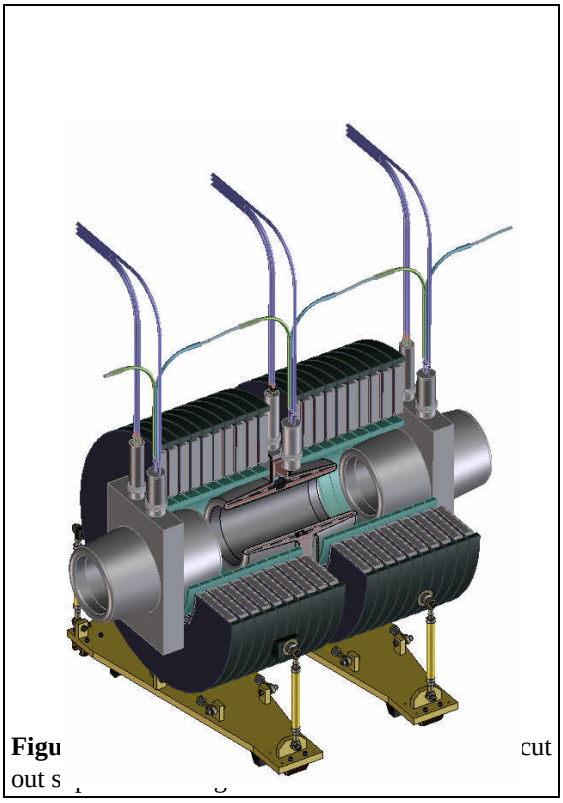

Figu cut out s

A cross section view of a pair of cells is shown in Figure 10. The bore radius of 20 cm corresponds to an axial magnetic field of 3.0 T. The induction cell's acceleration gap is 10 cm and its solenoid gap is 14 cm, which allows 2 cm per side for thermal isolation between the end of the superconducting coil and the vacuum feed conductor. The superconducting solenoid is 1.46 cm thick with an inside radius of 22.2 cm. The Mycalex insulator stack is 82 cm long by 5 cm thick with an inside radius of 36.4 cm. The induction cores are located outboard of the insulator with an inside radius of 45 cm and an outside radius of 77 cm.

5.3.2 Electric Field Stresses

An equipotential plot of the electric field distribution in the induction cell is shown in Figure 11. The field in the oil dielectric, radial feeds between individual cores is 150 kV/cm or 42 % of the calculated breakdown strength of 345 kV/cm. The peak axial field along the Mycalex insulator is 23 kV/cm for an effective stress time of 50 ns (89% of peak). This value compares to a measured breakdown field of > 33 kV/cm for a 2.2 μs pulse on the Mycalex insulator of the DARHT 2nd axis injector, which scales to >55 kV/cm at 50 ns (33 * (1000 ns/50 ns)$^{1/6}$). On the DAHRT and AIRIX 1st axis injectors vacuum cathode surfaces have been operated in a non-emitting mode at fields of 250 kV/cm, pulse lengths of 60 ns, and areas of 1000 cm^2. With some preliminary cathode conductor shaping the peak field in the accelerating gap is only 183 kV/cm, and in the region where emitted electrons could impact the insulator it is further reduced to 103 kV/cm.

5.3.3 Induction Cell Cores

Each 2.0 MV cell contains 10 individual 200 kV cores. Diametrically opposed cables drive alternate cores, and these core pairs are then clocked azimuthally to provide clearance for the pulse shaping network enclosures that couple the cables to the cell.

The induction cores provide the dominant load to the pulse train generator (2.5 kA of core current versus ~0.1 kA of beam current). Minimizing the core losses reduces pulsed power system costs, but lower core losses require the use of either more expensive core material or larger core volumes. The results of a scan which optimizes system costs are summarized in Table 3. Two types of Metglas manufactured by Allied Signal (USA) were considered, 2605SC and 2714A. 2605SC is the least expensive with the largest losses and 2714A is the most expensive with the lowest losses. A compromise between these extremes, which minimized system costs, was obtained with Finemet FT-1H, a nano-crystalline alloy manufactured by Hitachi (Japan) at a flux density swing of 1.0 T. This optimum gave a mean core loss current of 2.5 kA, which defined a core load impedance of 80 Ω used for the pulsed power design.

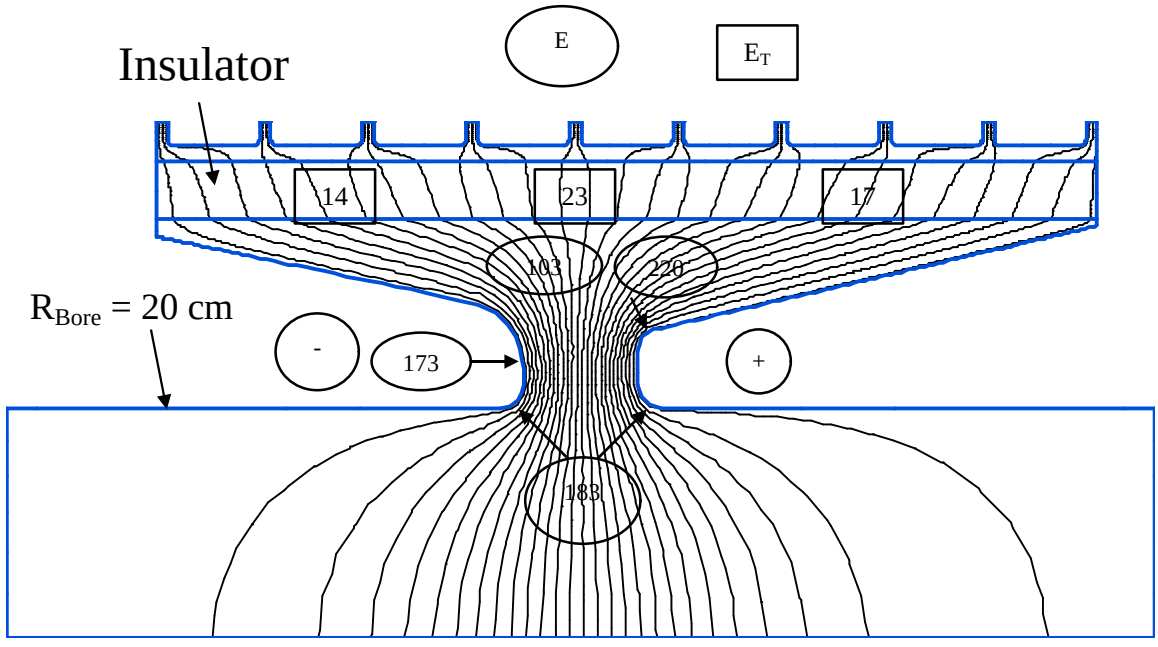

Figure 11: Cell Equipotential Plot. Electric Field Stress on the cell.

ΔV	V_{eff}	τ_r	τ_{flat}	τ_{eff}	$v\tau$	Type	δ	PF_r	ΔB_{max}	Cost	
kV	kV	μs	μs	μs	mV-s		gm/cc		T	Norm	
200	**142**	0.070	0.030	**0.07**	**12.6**	**Finemet**	7.32	0.70	**1.95**	**1.00**	**<-- Finemet**
200	**142**	0.070	0.030	**0.07**	**12.6**	**2605SC**	7.32	0.70	**2.90**	**0.36**	**<-- 2605SC**
200	**142**	0.070	0.030	**0.07**	**12.6**	**2605SC**	7.32	0.70	**1.10**	**2.00**	**<-- 2714A**

ΔB	A_{Met}	A_{Core}	$\Delta B/\Delta t$	L		Δr	r_i	r_o	r_o / r_i	r_{Mean}	H	I_{Core}	E_{core}	k	U_{Met}	V_{Met}	W_{Met}	System $
T	cm^2	cm^2	T/μs	"	cm	cm	cm	cm	cm	cm	kA/m	kA	J	J-μs/T-m^3	J/m^3	cm^3	kgm	Norm
0.97	130	185	**13.2**	2.28	5.8	32.0	45	**77**	1.71	61.0	0.65	**2.50**	31.5	**107**	**634**	49670	363.6	**1.00**
0.82	154	220	11.1	2.28	5.8	37.9	45	**83**	1.84	64.0	0.55	**2.23**	28.1	107	454	61744	452.0	1.02
1.48	85	122	20.1	2.28	5.8	21.0	45	66	1.47	55.5	0.98	3.41	42.9	107	1445	29688	217.3	1.07
0.82	154	220	**11.1**	2.28	5.8	38.0	45	**83**	1.84	64.0	0.98	**3.94**	49.6	**282**	**801**	61946	453.4	**1.13**
2.20	57	82	29.8	2.28	5.8	14.1	45	59	1.31	52.1	2.53	8.28	104.4	282	5571	18736	137.1	2.07
0.82	154	220	**11.1**	2.28	5.8	38.0	45	**83**	1.84	64.0	0.37	**1.50**	18.9	**41**	**306**	61946	453.4	**1.35**
0.86	147	209	11.7	2.28	5.8	36.1	46	82	1.79	64.1	0.39	1.59	20.0	41	339	58981	431.7	1.33

Table 3: Summary of Induction Core Parameters.

5.3.4 Superconducting Magnet for the Induction Cell

The requirements for the phase rotation linac solenoids are as follows: 1) the solenoid outside diameter should minimized. This means that the magnetic induction in the channel should be maximized. 2) The radial thickness of the solenoid cryostat should also be minimized. This allows the induction linac acceleration structure to be brought closer to the axis of the machine. As the magnetic field increases, the thickness of the superconducting magnet that creates the field must also increase. 3) The space between the induction linac cells must be minimized. This means that the space used for the cold mass support system, the electrical leads and the cryogen feed system

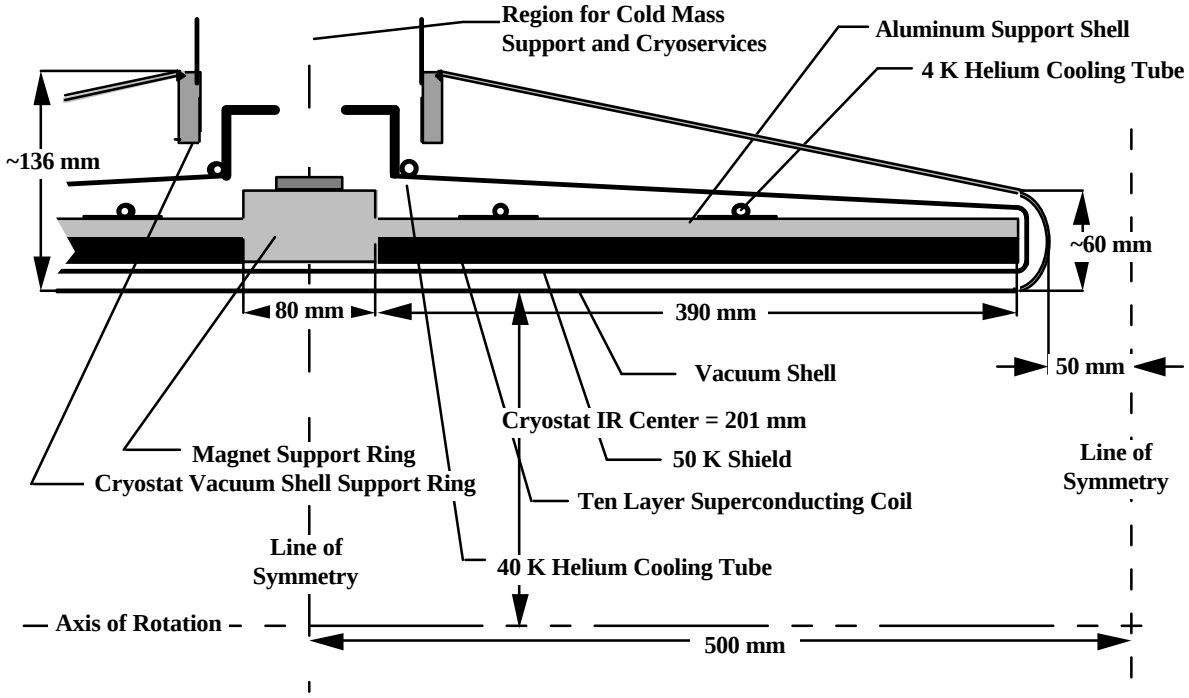

Figure 12: A cross-section of the Induction Linac Superconducting Coil and Cryostat

must fit in this minimum space. To further reduce the space occupied by the cryostat, the solenoid was designed to be cooled indirectly using flowing two-phase helium in a cooling tube attached to the support structure. The 40 K helium used to cool the shield is carried in tubes attached to the shields.

Figure 12 below shows a cross-section of a superconducting solenoid that is designed to generate an average induction of 3 T on the axis of the phase rotation linac. The inner bore of the solenoid cryostat is 400 mm. This allows a 200 MeV muon beam with a nominal diameter of 384 mm (at 3 T) to pass through the solenoid without loss (except from muon decay). The distance from the end of the superconducting coil to the outside end of the cryostat can be reduced to 20 mm. If an additional support clip is needed at the end of the coil, it can be accommodated in the space shown.

Magnet Physical Parameters	
Induction Linac Cell Length (mm)	1000.0
Magnet Cryostat Length (mm)	900.0
Magnet Coil Package Length (mm)	860.0
Number of Coils in the Coil Package	2
Length of Each Superconducting Coil (mm)	390.0
Inner Cryostat Radius (mm)	201.0
Superconducting Coil Inner Radius (mm)	224.3
Superconducting Coil Thickness (mm)	14.55
Support Structure Thickness (mm)	12.7
Magnet Cryostat Thickness at Ends (mm)	60.0
Magnet Cryostat Thickness at Center (mm)	136.0
Cold Mass per Magnet Cell (kg)	247.0
Overall Mass per Magnet Cell (kg)	292.0
Magnet Electrical Parameters	
Average Central Induction (T)	3.00
Peak Induction in the Windings (T)	~4.5
Number of Turns per Cell	4580
Magnet Design Current (A)	521.27
Magnet Design Operating Temperature (K)	4.4
Conductor Critical Current at Operating T (A)	~790
Magnet Stored Energy per Cell E (kJ)	618
Magnet Self Inductance per Cell (H)	4.55
Superconductor Matrix J (A mm^{-2})	331
E J^2 Limit per Magnet Cell (J A^2 m^{-4})	6.76×10^{22}

Table 4: Phase Rotation Solenoid Parameters.

The proposed conductor for the coil shown in Figure 12 above is a standard MRI magnet conductor that is 1 part NbTi and 4 parts RRR=70 copper. This conductor has fifty-five 85-μm filaments twisted with a twist pitch of 12.7 mm. The bare matrix dimensions of the conductor are 0.955 mm by 1.65 mm. The insulation on the conductor is 0.025 mm thick. At an average design induction of 3.0 T on axis, the coil design current is about 521.3 A. As a result, the coil would be a 10 layer coil that is 14.6 mm thick (including 2 mm of ground plane insulation).

It is proposed that the coils be wound and cast on a form that is removed after the coil is cured. After curing the coils are removed from the mold and machined at the ends and on the outer radial surface. After the coils are machined they can be shrunk fit into a 6061 aluminum support structure that has been machined so that the coils closely fit with in it. Table 4 on the next page shows the design parameters for the induction linac solenoids.

The 6061-aluminum support structure on the outside of coils serves the following functions: 1) It limits the coil strain by carrying some of the magnet hoop forces, and 2) it serves as a shorted secondary to protect the magnet during a quench. A single magnet is entirely self-protected through quench back from the support structure. One can use quench back to protect a string of these magnet as well. When a quench is detected in one magnet, the current in the string can be discharged through a varistor resistor, causing all coils to go normal through quench back from the support structure.

The space available longitudinally for leads, cryogenic services and cold mass supports is about 85 mm wide at the center of the magnet. The cold mass of phase-rotation solenoid (including the 40 K shield and lower lead assembly) is estimated to be about 250 kg. The primary forces that will be seen between the cold mass and room

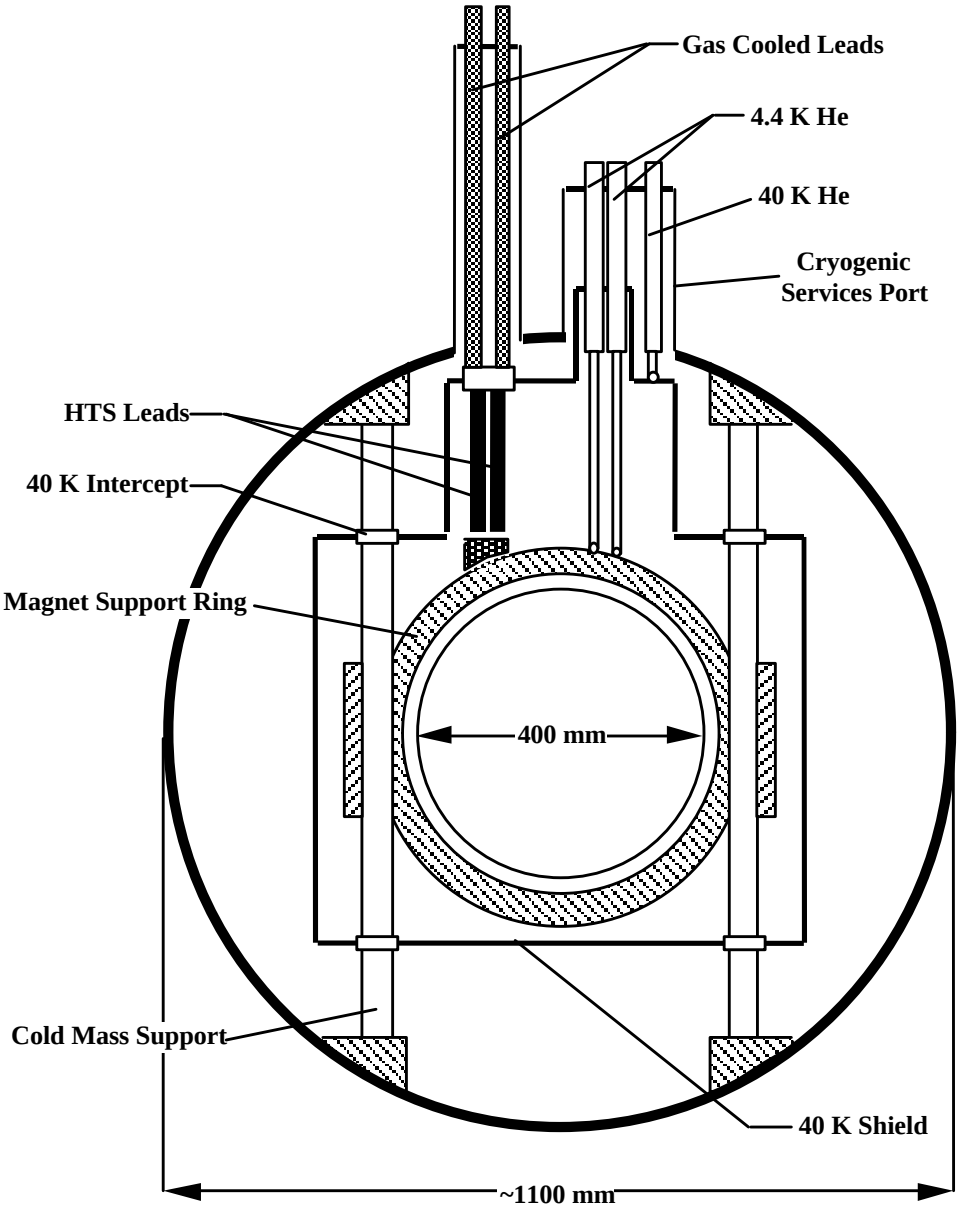

Figure 13: Induction Linac Solenoid Cold mass Support System and Leads.

temperature will be forces do to shipping and forces introduced due to unbalanced magnetic fields. The magnet cold mass supports are designed for a force of 10000 N in any direction. It is proposed that a pair of 60 mm diameter oriented carbon fiber tubes (with a wall thickness of about 3 mm) be used to carry forces from the cold mass to room temperature.

Since there is a solenoid magnet every meter down the phase rotation channels and the drift spaces between the phase rotation linac sections, leads must be brought out of each of these magnets. One has two choices: 1) All of the magnets or 20 to 25 meter long subsets can be hooked in series and run off of a common power supply. Inter-connects between the solenoids can be either superconducting or conventional copper cable. 2) Each magnet can have its own set of leads to room temperature and its own power supply, so individual cells can be tuned. It is proposed that the leads between 4 K and 40 K be made from high temperature superconductor (HTS). The leads from room temperature to the top of the HTS leads at 40 K should be gas-cooled. Gas from the refrigerator that is

used to cool the magnet shields and cold mass support intercepts can be used to cool the gas-cooled leads. This gas must be returned to the refrigerator compressor intake at room temperature. Figure 13 shows a schematic representation of the cold mass support system, the helium supply system, and the current leads.

The induction linac superconducting solenoids are cooled by conduction from the 6061-aluminum support structure. The aluminum support structure will be cooled by two-phase helium flowing in tubes attached to the support structure. Two-phase helium cooling is commonly used to cool detector magnets and magnets that are used in physics detectors. The advantages of two-phase tubular cooling are as follows: 1) There is very little helium inventory within the magnet. 2) The two-phase helium tubes have a high-pressure rating. This means that the magnet cryostat is not a pressure vessel. 3) Two-phase helium cooling does not require a cold compressor or a helium pump to circulate the helium through the magnet cooling system. 4) The helium in a two-phase helium cooling circuit decreases as along the flow circuit. 5) The pressure drop along a two-phase helium flow circuit is lower than for a supercritical helium flow circuit. A large number of superconducting solenoid magnets have been cooled using force flow two phase helium in tubes.
It is assumed that the magnet shown is one of twenty to twenty-five magnets that are cooled in series from the two-phase helium refrigerator and control cryostat. If twenty to twenty-five magnets are cooled, the mass flow rate through the flow circuit should be about 2.5 grams per second. The two-phase helium tube would be attached to the superconducting coil support structure, the base of the HTS leads and the attachment points of the cold mass supports. The heat that is added to the two-phase helium flow stream in each of the solenoid is expected to be about 0.5 W.

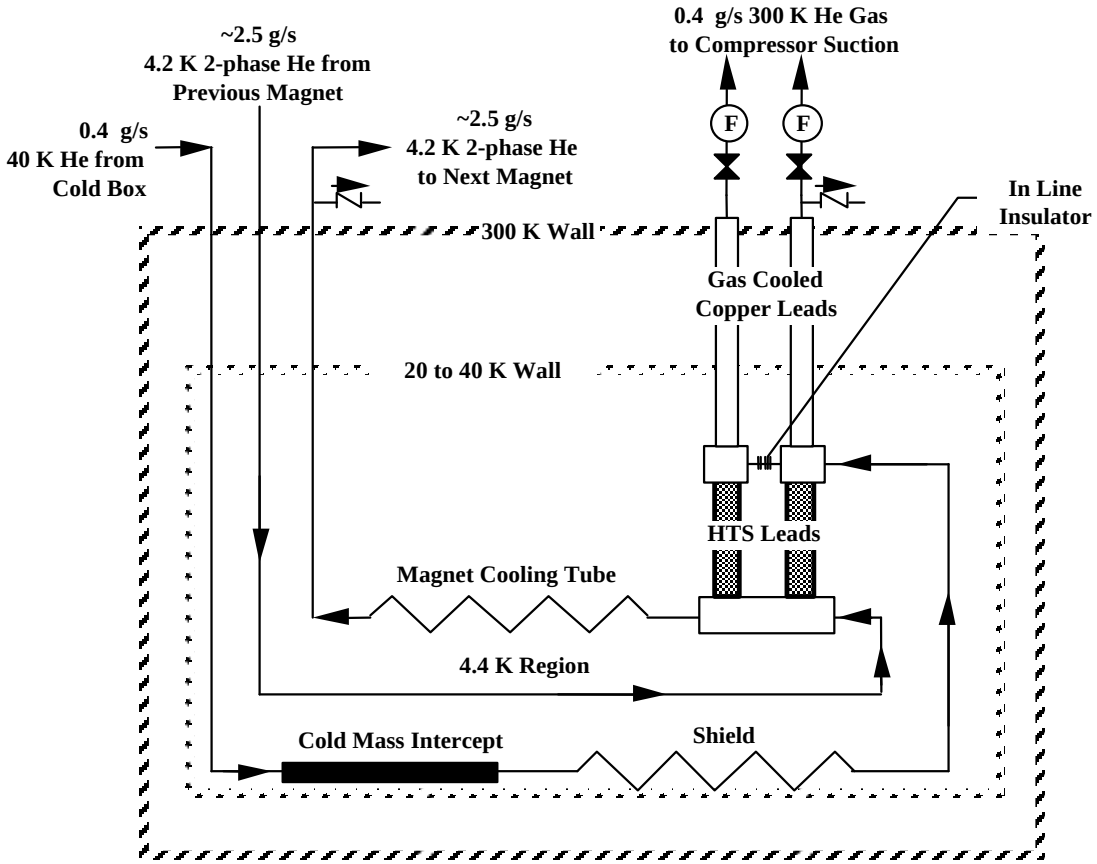

Figure 14: Cryogen Distribution within the Induction Linac Solenoid Cryostat.

5.3.5 4 Pulse per Booster Cycle System Architecture

The pulser system is certainly the most ambitious piece of hardware for the induction linac layout. While single pulse a comparatively easy to provide, multiple pulses at the required voltage rating are difficult to produce. Although two approaches have been considered, the first one presented here is our present baseline. Figure 15 represents a layout of the pulsed power system showing the major components to scale. They consist of cell cables, a water dielectric delay line, four series pulse forming lines, PFLs, magnetic compressor pulse charge modules, MCPCs, and a thyristor switched prime power unit. One of these units is required per induction module, overall 100 of them.

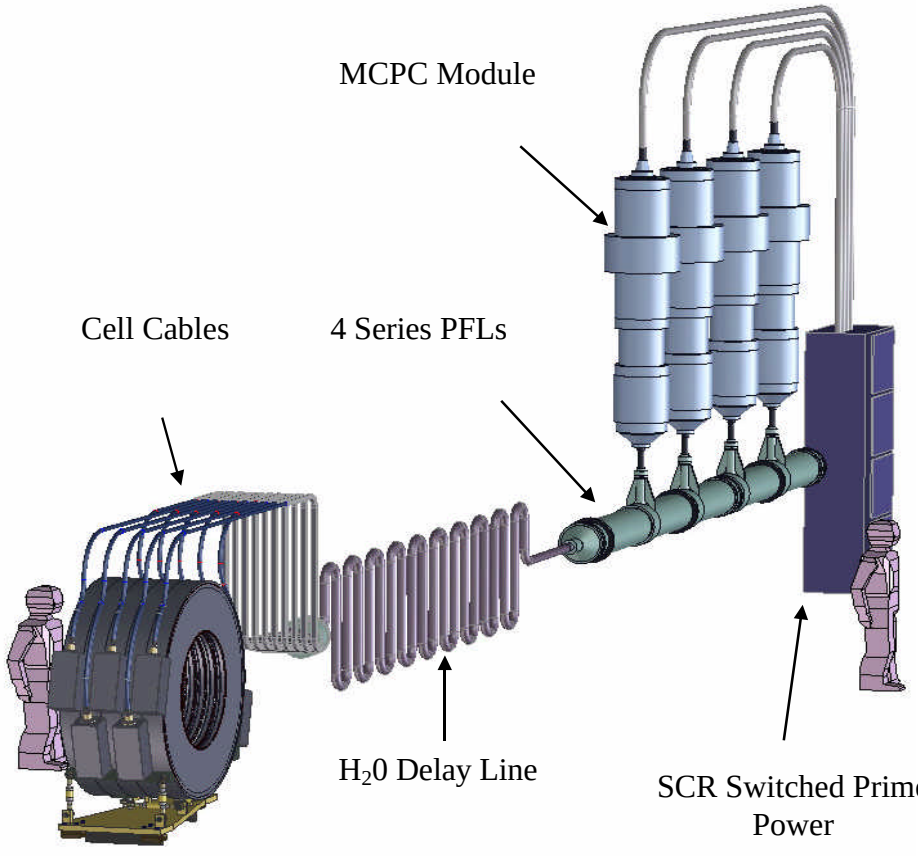

Figure 15: Pulsed Power System layout

Figure 16 is a block diagram of the system that documents key parameters of the components. The generation of four bipolar, 100 ns pulses spaced 400 ns apart is made possible by the use of rapid cell core reset that returns them to the same state between the pulses. 8.3 kA of cell reset current is supplied via a 17 μH inductor housed in a cable adapter at the end of the water delay line. The inductor energy is supplied in 220 μs by a simple Thyristor switched capacitor bank (72 μF at 4.0 kV). The reset current resets the cell cores towards – saturation, blocking leakage current from the four pulse generator, and allowing voltage to develop across the accelerating gap. A + 1.5

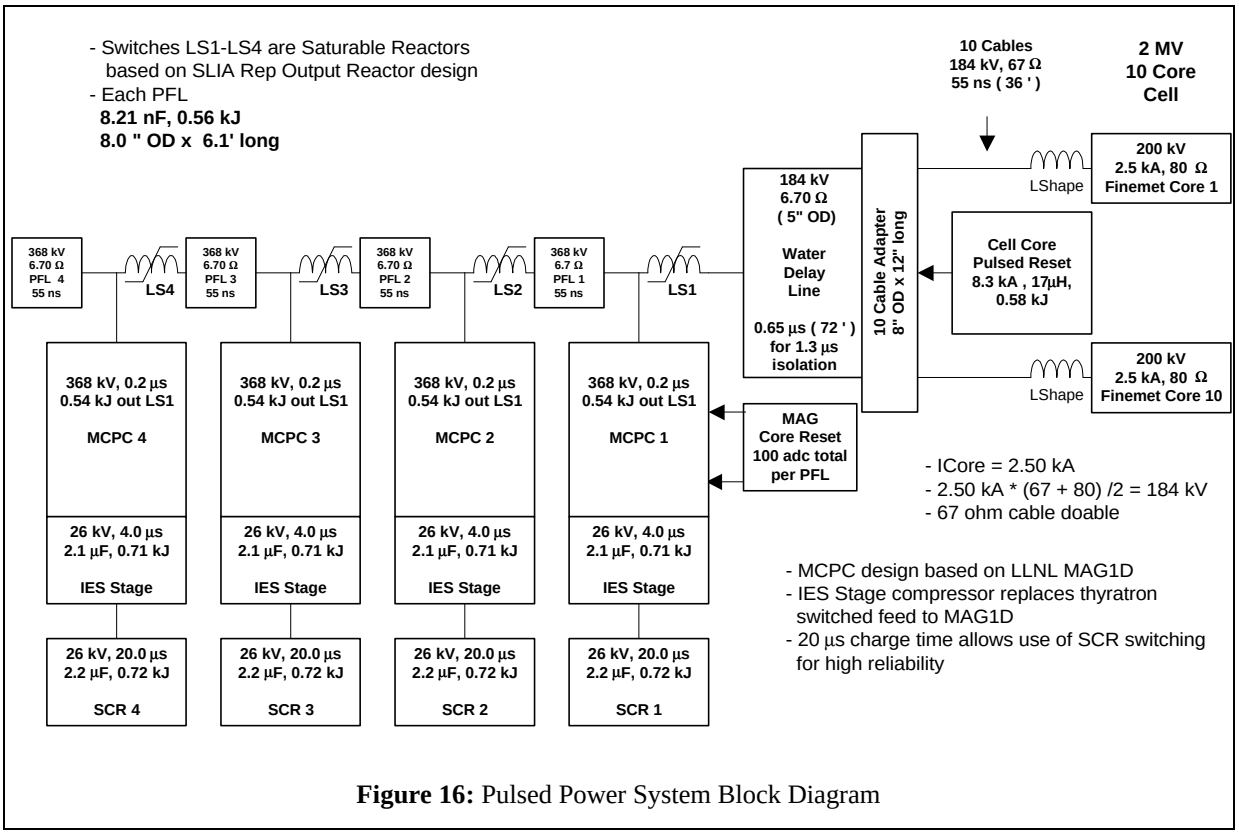

Figure 16: Pulsed Power System Block Diagram

MV pulse from the 4 pulse generator drives the cores towards + saturation. When the pulse disappears, the reset current produces –0.5 MV across the accelerating gap while providing rapid seset of the cores in preparation for the next pulse. Without rapid reset the core area would have to be a factor of four larger, a significant cost impact, and the pulse generator would have to produce the bipolar pulse. It is desirable that the volt-second product of both the acceleration pulse and the reset pulse be equal so that the cell cores are in the same state for each pulse to ensure pulse to pulse reproducibility. Even more importantly the reset pulse must not drive the cell cores completely into saturation before the arrival of the next acceleration pulse or the head of the beam will see 0.0 MV instead of –0.5 MV. The reset pulse width must also be at least 3 times the acceleration pulse width to allow switching transients from the pulse generator to be damped out to an acceptable level. These criteria lead to the asymmetric bipolar acceleration pulse and a net acceleration of 0.5 MV per cell. They also lead to the addition, of a pre-pulse generator not shown in Figure 15 and Figure 16 that will be attached in parallel with LS1 at the entrance to the delay line. Without it, the cell cores would be at – saturation when the first pulse arrived, because of the long time scale of the reset circuit. The pre-pulse generator will supply a > 8.3 kA pulse to the cell cores to overcome the reset current, and drive the cores towards + saturation past their desired operating point. When this +80 kV, 100 ns long pre-pulse ends 100 ns before the beginning of the 1st pulse, the reset current will develop – 50 kV across each cell core and return the cores to the desired operating point for the start of the 1st pulse. The pre-pulse PFL energy is only 42% of the individual main pulse PFLs.

The 1st pulse of the 4 pulse train is generated by the closure of the saturable reactor LS1, which discharges PFL1, launching a 184 kV, 100 ns square wave pulse with a 20 ns risetime into the water dielectric delay line. At the end of the delay line the pulse is routed via ten 67 Ω cables to the ten 80 Ω cores of the cell. The cable to core mismatch developes a change in core voltage of 200 kV superimposed on the reset voltage of –50 kV. The pulse shaping networks at the cable/cell interface convert the fast risetime square wave to the required hyperbolic shape. For this study a simple inductor was used to approximate the required shape. The delay line prevents first pulse reflections from this mismatch from returning to the cell for the pulse train length of 1.3 μs. Once discharged, PFL1 acts as a matched output line for the PFL2 when LS2 closes launching the 2nd pulse into the delay line 400 ns later. The sequence repeats until the 4th pulse of the train is generated by closure of LS4. The risetime of the 4th

pulse is slowed to ~40 ns because it has to trnsverse the saturated inductance of 4 switches, but this is largely compensated for by the pulseshaping network at the cell.

Each series PFLs is pulse charged to 368 kV by a MCPC. For this study the MCPC design was based a MAG1D currently in use at 1 pule per second at LLNL so that realistic costs could be developed. A modified version of a MAG1D was run at 100 Hz at PSI. As part of the R&D effort the MCPC design would be optimized for this application. An intemediate energy store, IES, magnetic compression stage was added to the back end of the MAG1D to replace its thyratron switched feed. Extension of the charge time from 4.0 μs to 20 μs allows the use of commercially available thyristors for high reliability switching.

5.3.6 Preliminary Circuit Simulations

A simple circuit simulation of the four series PFLs with realistic saturated switch inductances, the delay line, cables, simple inductor waveshape network, and a resistive load for the core was done to check the feasibility of producing the required pulse waveshape with this approach. Figure 17 shows a four pulse train of the square-wave injected into the delay at the top and the cell voltage on the bottom. Although the 4th pulse of the top pulse train shows significant distortion on the top of the waveform and a slower risetime, much of this is integrated out on the core voltage waveform. Figure 17 shows an overlay of the 1st and 4th pulse of the core voltage pulse train with the

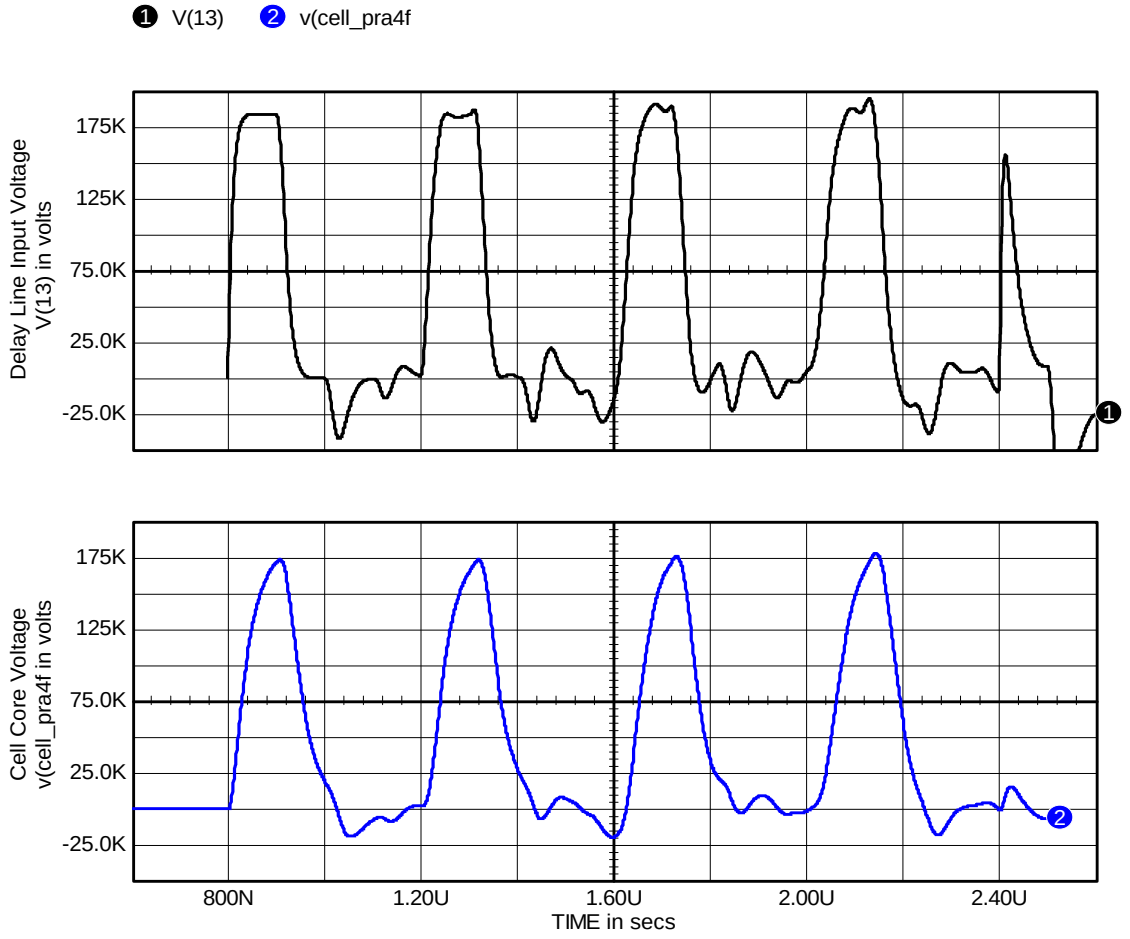

Figure 17: Delay Line & Core Pulse Train Voltage Waveforms

pulses time shifted for comparison. Based on these results it seems reasonable that a combination of rear PFL impedance tailoring and special pulse train generators along the Induction Linac will allow matching of the four pulses in the train.

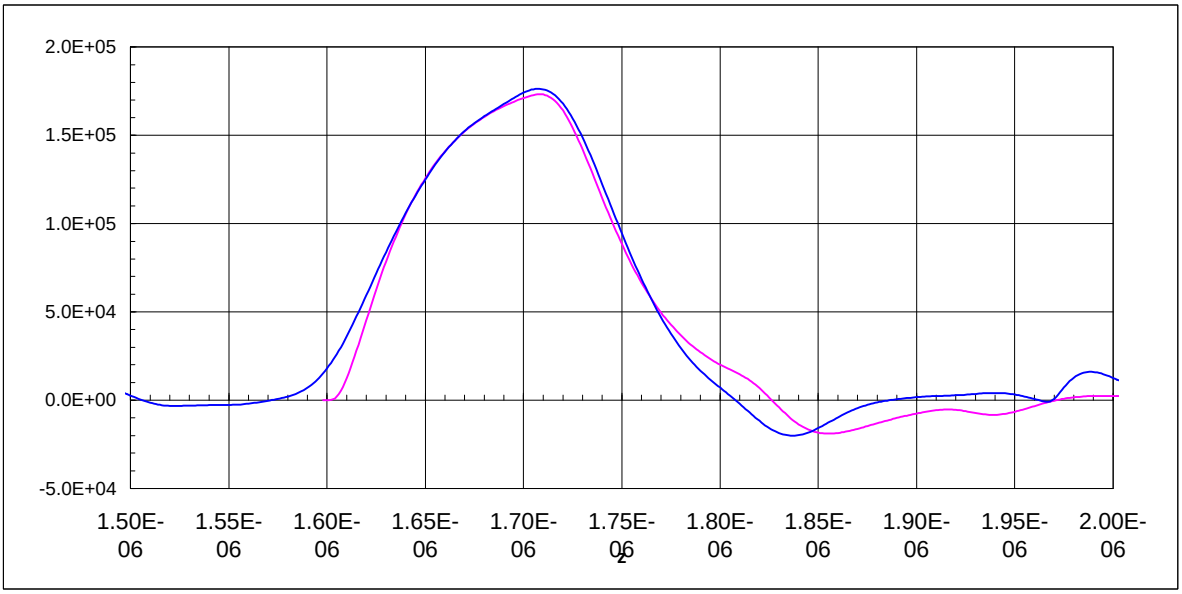

Figure 18: Overlay of the 1st & 4th Pulse of the Train

5.3.7 Alternative Approach for the Pulsing System

A second design for the pulser system was initiated in order to investigate alternative methods for generating the power pulse driving the induction cores. Figure 19 shows a simplified electronic layout for the pulse power generator[4]. The inductor voltage is formed by the common discharge of the forming capacitor C0 and pulse

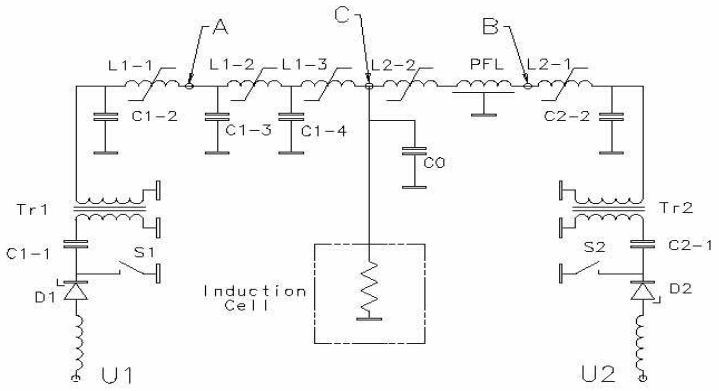

Figure 19: Conceptual scheme of the voltage pulse power generator.

forming line (PFL) into the inductor. A detailed scheme description is provided in [7], and the resulting pulse shape is shown in Figure 20. For this power system approach, LIA accelerating gradient changes from -1.5 MV/m in the beginning of the cycle to 0.5 MV/m in the end, which is similar to what was found optimal in [5]. The time duration of the negative and the positive parts of the voltage pulse are chosen so that the volt-second areas are equal. As a result, magnetic reset of the induction cell core is reached automatically, and after one voltage pulse ends, the system is ready to accept the next one. This power system approach allows generation of several pulses by adding fast charging circuits in parallel at points A and B in Figure 19.

The impedance of the circuit in Figure 19 can not be made arbitrarily small. Nevertheless, it appears possible to use one generator to feed ten inductors (0.5-m of total length) in parallel. Core power loss is the major factor that dictates the size and the cost of a pulsed power system. It was shown in [6] that it is important not to underestimate core power loss because it scales nonlinearly with applied voltage. In order to calculate the average power loss, careful calculation of the instant power loss has to be made followed by integration over the pulse length. Calculations made according to this scheme resulted in a minimal induction core weight of about 100 Tons and an average power required for the total system of about 5 MW. The next step of the development will include thorough simulation of pulsed power circuits that take the nonlinear induction cell impedance into account, as well as stray inductance, and stray capacitance of each section element.

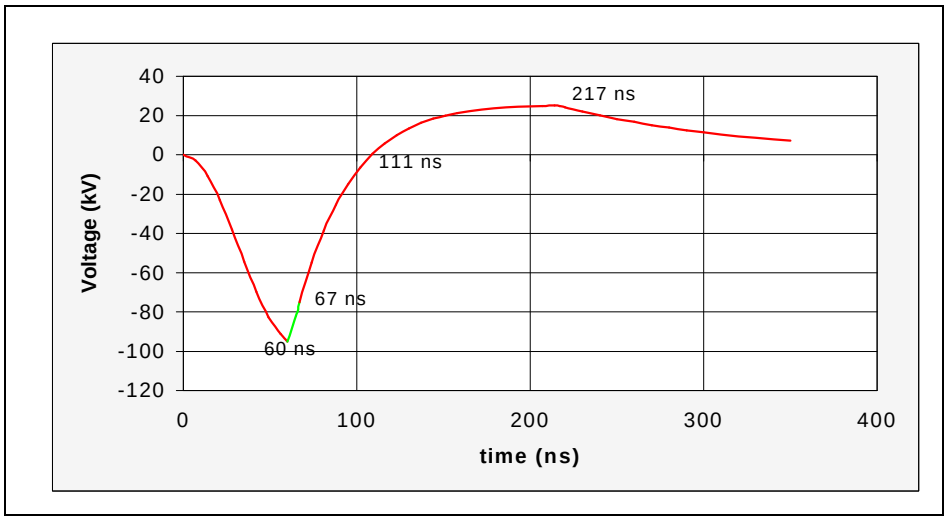

Figure 20: Output voltage pulse applied to an inductor in the LIA section.

5.4 Summary

The reduction of the energy spread of the muon beam is the primary goal of this phase rotation section. The central component that provides the necessary time dependent voltage, is the induction linac. All the other technical components (solenoids in the decay channel, mini cooling absorber, buncher cavities) are simple compared to the induction linac. The superconducting coils inside the induction cores are an additional technical complication. The assessment of all these difficulties and the initial design approach being presented here indicate that the technical problems are solvable with a reasonable amount of R&D.

The phase rotation design presented here performance of the phase rotation on the other hand, as being presented here, meets our intensity performance goal, however the energy spread is still too large in order to guarantee good performance through the buncher section and the cooling channel. More work is needed.

REFERENCES

[1] C. Ankenbrandt et al., "Status of Muon Collider Research and Development and Future Plans", Phys. Rev. ST Accel. Beams 2, 081001 (1999)

[1] S. Geer, C. Johnstone, and D. Neuffer, “Muon Storage Ring Neutrino Source: The Path to a Muon Collider?", FN-2073, March 1999.
[2] V. Balbekov, “Pre-cooling Stage of Neutrino Factory”, MUCOOL note 96, March 2000.
[3] V. Balbekov, “Optimization of Phase Rotation Using an Induction Linac”, MUCOOL note 63, October 1999
[4] J. Fockler et al., “Induction Linac Technology for Muon Beam Phase Rotation”, Neutrino Factory Feasibility Study Workshop, February 2000.
[5] Terechkine, “Neutrino Factory Phase Rotation LIA: Pulsed Power System Optimization”, January 2000 http://www.fnal.gov/projects/muon_collider/nu-factory/subsys/ss-phrot/Optimization.pdf.
[6] S. Yu, LBNL, private communication, Jan. 2000.
[7] V. Kazacha, A. Sidorov, I. Terechkine "Pulsed Power System of Linear Induction Accelerator for FNAL Neutrino Factory".http://www.fnal.gov/projects/muon_collider/nu-factory/subsys/ss-phrot/proposal_inductl.pdf.
[8] D. Neuffer, “RF Capture Variations for the Muon Collider Neutrino Source”, MUCOOL note 52, October, 1999.
[9] A. Van Ginneken, unpublished, January 2000.
[10] R. B. Palmer, C. Johnson, and E. Keil, “A Cost-Effective Design for a Neutrino Factory”, MUCOOL-67, November 1999, Proc. NuFact99, Lyon, 1999.
[11] Bob Palmer, The draft of the current results of this paper are now at <http://pubweb.bnl.gov/people/palmer/nu/pjksim/pjksim.ps>, and will appear shortly as a MUC note.
[12] W. Chou and A. Van Ginneken, “Phase Rotation Using Low-frequency RF”, MUCOOL note 90, February 2000.